Light Element Abundance Inhomogeneities and Deep Mixing in Galactic Globular Clusters

Jeffrey Gerber and Michael Briley

Appalachian State University

525 Rivers St.

Boone, N.C, 28608

gerberjm@appstate.edu and brileymm@appstate.edu

Received ______________________; accepted ______________________

ABSTRACT

It was discovered some thirty years ago that stars in Galactic globular clusters tend to decrease in carbon abundance with increasing luminosity on the red giant branch, particularly among the lower metallicity clusters. While such a phenomena is not predicted by canonical models of stellar interiors and evolution, it is widely believed to be the result of some extra mixing operating during red giant branch ascent which transports material exposed to the CN(O)-cycle to the surface.

Here we present an analysis of observations in the evolving red giants of globular clusters within our own Galaxy. Building on the work of Martell, Smith, and Briley (2008, AJ, 136, 2522), we have used the KPNO 4-m and SOAR 4.1-m telescopes to extend the sample of clusters. The CH absorption features in these low resolution blue spectra have been analyzed via synthetic spectra in order to obtain [C/Fe] abundances. These abundances and the luminosities of the target stars were used to establish the rate at which C abundances are changing with time (i.e., the mixing efficiency). By establishing rates over a wide range of composition, the dependence of deep mixing on metallicity can be determined and used to better constrain theories of the underlying process. We find that not only do our carbon rates decrease as a function of metallicity as expected, but the carbon rates are heavily dependent on the initial [C/Fe] composition of the star.[1]

Subject headings: globular clusters: general – stars: abundances

[1]This publication makes use of data products from the Two Micron All Sky Survey, which is a joint project of the University of Massachusetts and the Infrared Processing and Analysis Center/California Institute of Technology, funded by the National Aeronautics and Space Administration and the National Science Foundation.

1. Introduction

It is known that the mean [C/Fe] abundance of red giant stars in globular clusters (GC) decreases as the stars increase in luminosity on the red giant branch (RGB). This phenomenon defies canonical stellar models that predict surface abundances to be static after the first dredge-up due to a radiative zone between the hydrogen burning shell and the surface. Nonetheless, progressive deep mixing in evolving RGB stars, where carbon-depleted material from the hydrogen-burning shell undergoing the CN(O) cycle is brought to the surface, has been used to explain the carbon depletion observed (Sweigart & Mengel 1979).

Furthermore, this deep mixing only occurs in RGB stars that have evolved farther than the luminosity function (LF) bump on the color-magnitude diagram for the cluster (Charbonnel, Brown, & Wallerstein 1998). The LF bump is a result of a stutter in the evolution of the star when the hydrogen burning shell around the core advances outwards and encounters a large difference in the mean molecular weight (μ-barrier). The μ-barrier is left behind from the first dredge up that occurs during the evolution of the star just after the subgiant phase.

During the first dredge up, the convective envelope of the star moves inward in mass as the core begins to contract. The inward movement of the convective envelope causes partially processed material of the stellar interior to become mixed with unprocessed material at the surface. As hydrogen burning in a shell around the core continues, the temperature gradient near the core increases and forces the base of the convective envelope outwards. The μ-barrier is left behind at the greatest point of inward progress of the convective envelope (Iben 1965).

Later, as the hydrogen burning shell begins to expand, it encounters the μ-barrier and the sudden influx of the hydrogen-rich material brought from the surface of the star causes the star to become bluer and fainter. The star then reaches equilibrium again and continues to evolve up the RGB (Iben 1968). In a collection of stars that have a very similar age and initial composition (as found in GC's), the effect of this evolutionary stutter is seen as a large number of stars all at the same magnitude, which creates the LF bump.

For higher-metallicity stars, the base of the convective envelope is driven lower during the first dredge up phase, which means the hydrogen burning envelope will reach the μ-barrier earlier in the evolution up the RGB. Because the μ-barrier is reached earlier in the evolution of the star, the luminosity function bump will therefore occur at a lower luminosity for clusters with higher [Fe/H] abundances (Zoccali et al. 1999).

The exact physics behind the deep mixing process causing the carbon depletion of RGB stars is not entirely known although multiple models have been suggested. Canonical stellar models do not usually incorporate a mechanism that is capable of transporting material across the radiative zone found between the hydrogen burning shell and the convective envelope. In 1979, Sweigart & Mengel developed a model of deep meridional circulation within the radiative zone induced by stellar rotation. Recent drivers of a deep mixing process such as Rayleigh-Taylor (Eggleton, Dearborn, & Lattanzio 2006) or thermohaline instabilities (Charbonnel & Zahn 2007; Denissenkov & Pinsonneault 2008) have been considered. However, all of these mechanisms are sensitive to the μ-barrier discussed above, which is dependent on [Fe/H]. The rate of carbon depletion (or the efficiency of mixing) is expected to be a function of [Fe/H] and, therefore, a fundamental constraint on deep mixing and is necessary for testing the suggested models.

For this project, we studied carbon depletion rate as a function of metallicity in GC RGB stars that have surpassed the LF bump in their evolution. A sample of stars were observed from multiple GC's with a range in [Fe/H] values. The carbon depletion rate for each star was determined based on the [C/Fe] abundance and change in luminosity as a function of time found using isochrones. A similar method to the one used in this study is discussed in Martell, Smith, & Briley (2008). The observations and results are discussed below.

2. Observations

Evolved giants from multiple clusters were chosen to create a sample with a range of metallicities. The sample consists of 71 stars in total chosen from various photometric surveys with 11 from observations made using the Southern Astrophysical Research Telescope (SOAR) and 60 from observations made at Kitt Peak National Observatory (KPNO). The stars in this sample were chosen to have an absolute magnitude of $\sim$ -1.5 in order to guarantee that the stars were surficiently beyond the luminosity function bump for the cluster, but still distinguishable from AGB stars.

2.1. SOAR Data

The observations from SOAR utilized the Goodman High Throughput Spectrograph on the 4.1-m telescope. The spectra have a 2.3Å full width half maximum and cover from the blue cut-off to 6200Å. The spectrograph used a 600 l/mm diffraction grating. For each star, 2-3 exposures were taken to provide 1800s of total exposure time. Poor weather conditions limited the observing time to 2.5 nights instead of the intended 3. A square root of the count just red of the CH band in each spectrum was taken to approximate the signal to noise ratio for the spectra. Each spectrum had a signal to noise ratio of $\sim$50. A sample spectrum is shown in Figure 1.

2.2. KPNO Data

The observations from KPNO used the 4-m Mayall telescope with the R-C Spectrograph. The spectrograph used the KPC-007 grating, which has a 4Å FWHM and cover from blue cut-off to 5500Å. For each star, 1-2 exposures were taken for 900-1800s of total exposure time. The observations were made over four nights from June 10-14, 2010. Each spectrum had a signal to noise ratio of $\sim$30. A sample spectrum is shown in Figure 2.

3. Analysis

The spectra for each star from the KPNO observations were reduced following the standard reduction procedures using IRAF.[2] The radial velocities for each star were calculated by cross-correlating the stellar spectrum with a synthetic spectrum of a typical red giant to check for membership.

For the SOAR observations, a different method was used to reduce the spectra due to a large reflection in the flat field images obtained from the telescope. To eliminate the reflection, a series of flats were taken at a different grating angle which moved the reflection to a different location in the image. The region in the original flat with the reflection was then replaced with a section from the new flat (after normalization).

Another problem encountered with the SOAR observations was that all of the arc lamp exposures taken for each spectrum were underexposed. Here a well exposed arc was used to obtain the general shape of the pixel-wavelength solution which was then applied to the program stars. A cross-correlation between the resulting program spectrum and a synthetic template was used to shift the observed spectrum into the rest frame. While a consequence of this approach was the loss of any radial-velocity information, the program stars are believed to be program members based on their locations in the cluster color-magnitude diagrams and the appearance of their spectra.

The indices used to find the carbon abundances for each star were sensitive to the S3839 CN absorption band (located at 3883Å) and the CH absorption band (located at 4300Å). The S3839 CN band index used compares the intensity in the blue CN band at 3883Å with the nearby continuum (Norris et al. 1981). The iCH absorption band index used has a blue continuum bandpass from 4180 Å to 4250 Å, and a red continuum bandpass

---

[2]IRAF is distributed by the National Optical Astronomy Observatory, which is operated by the Association of Universities for Research in Astronomy (AURA) under cooperative agreement with the National Science Foundation.

from 4380 Å to 4460 Å. The feature bandpass for the band covers the wavelengths 4285 Å to 4315 Å (Cohen 1999).

The model atmospheres generated for each star were computed using MARCS (Gustafsson, Edvardsson, Eriksson et al. 2008) and the SSG synthetic spectrum generator (Bell, Paltoglou, & Tripicco 1994). The effective temperatures and surface gravities required for the stellar models were derived using the V-K colors for the star, its absolute magnitude, and an [Fe/H] value based on its cluster membership. V magnitudes for each star came from numerous sources depicted in Table 1. K magnitudes for each star came from 2MASS (Skrutskie, Cutri, Stiening et al. 2006). The [Fe/H] value was based on the published value from the Harris catalogue (Harris, W. E. 2010). The method used to determine the temperatures and surface gravities is described in Alonso, Arribas & Martinez-Roger (1999) and Alonso, Arribas & Martinez-Roger (2001).

The equation in Alonso, Arribas & Martinez-Roger (2001) that describes the effective temperature of a star as a function of the V-K color uses the Carlos Sanchez Telescope (TCS) system. Our V-K colors from 2MASS were converted to the TCS system using the method described in Johnson et al. (2004). The V-K color on the TCS system was then corrected for reddening by subtracting the reddening factor for the B-V color of the star from Harris, W. E. (2010) multiplied by 2.74, which is the adopted conversion factor from Prisinzano, L. et. al. (2012).

The synthetic spectra were calculated for each effective temperature and log(g) with the appropriate [Fe/H] then smoothed to match the observed spectrum for the individual star. Carbon and nitrogen were adjusted simultaneously to match the CN and CH indices. An [O/Fe] of +0.3, ξ of 2.0 km/s, and 12C/13C of 4.0 were assumed for the synthetic spectra. The resulting carbon abundances are plotted in Figure 3 as a function of the metallicity of the cluster. The [C/Fe] and [N/Fe] values are presented in Table 1.

The sensitivity of the resulting abundances to assumed values of [O/Fe], C12/C13, and errors in temperatures and gravities were assessed by repeating the C abundance determinations using different values. Their effect on the final C abundances are given in Table 2. The greatest sensitivity was to [O/Fe], which was expected due to the role of the CO molecule in molecular equilibrium.

4. Discussion

Figure 3 plots [C/Fe] versus metallicity for each star in the sample, which shows a large scatter. The reason for the scatter is that the [C/Fe] value for the star is dependent on its initial [C/Fe], the depletion rate of carbon from its surface, and how long the star has been mixing. The goal of this study was to produce a value for the carbon depletion rate of each star and compare it to the metallicity. This rate was expected to decrease with increasing metallicity.

In order to convert the carbon abundance of each star into a carbon depletion rate, the length of time since the star passed through the luminosity function bump (the expected onset of deep mixing) was found. The location of the luminosity function bump for each cluster was estimated using a relationship between the luminosity function bump of a cluster and its metallicity (Fusi Pecci et al 1990). A linear interpolation was used with the data from Fusi Pecci et al. (1990) to calculate a luminosity function bump value for each cluster studied in our sample. The data from Fusi Pecci et al. (1990) as well as the values found for our cluster sample are both shown in Figure 4.

Yale Y^2 isochrones were used to determine a value for a change in absolute magnitude as a function of time, $\Delta M_v/\Delta$t, for stars in each globular cluster (Yi et al. 2001). A model point was chosen within 0.05 mags to the luminosity function bump on an isochrone created with an age of 12 Gyr. New isochrones were then created at older ages until one was found where the model point had evolved to an absolute magnitude of -1.5 $\pm$ 0.05. These values provided a $\Delta M_v/\Delta$t, which represents the rate a star evolves up the RGB past the luminosity function bump in each cluster.

Once a change in magnitude as a function of time had been calculated for each star, a change in carbon abundance as a function of magnitude was determined by dividing the change in [C/Fe] (assuming an initial solar [C/Fe]) by the change in absolute magnitude of the star from the luminosity function bump of the cluster. With Δ[C/Fe]/ΔM_v established for each star in the sample, a value for the carbon depletion rate, Δ[C/Fe]/Δt, was determined by multiplying Δ[C/Fe]/ΔM_v and $\Delta M_v/\Delta$t.

Figure 5 is a plot of the carbon depletion rate for each star as a function of its metallicity, which demonstrates how the carbon depletion rate decreases as a function of metallicity. The result is similar to the result from Martell, Smith, and Briley (2008), but a large spread is seen in the depletion rate at each metallicity (especially around a [Fe/H] $\sim$ -1.5 where the sample is more dense).

To explore the wide range in carbon depletion rate, [N/Fe], determined by simultaneously fitting the CN band, was examined for each star to determine if the star was nitrogen strong or nitrogen normal. If a star is nitrogen strong, it indicates that during the star's formation it incorporated CN(O)-cycle material that was ejected from nearby AGB stars early in the cluster's history. While the CN(O)-cycle material is nitrogen enhanced, it has been depleted in carbon; therefore, nitrogen strong stars would generally have a lower initial carbon abundance than nitrogen normal ones. An analysis of a histogram of [N/Fe] for the sample showed two peaks separated at a [N/Fe] $\sim$ 0.95. Therefore, stars with a [N/Fe] greater than 0.95 in this sample were considered nitrogen strong, and those with a [N/Fe] less than 0.95 were considered nitrogen normal.

A plot of carbon depletion rate versus metallicity is shown in Figure 6 with the stars indicated as nitrogen strong or nitrogen normal. In general, it appears as though nitrogen strong stars have higher carbon depletion rates than nitrogen normal ones. However, the carbon depletion rates are overestimated for the nitrogen strong stars because their initial carbon abundances are actually lower than assumed in the calculation of Δ[C/Fe]. If the initial carbon abundance is lowered to -0.3 for the nitrogen strong stars, Δ[C/Fe] is reduced as well as the carbon depletion rate. Lowering the carbon depletion rates in the nitrogen strong stars reduces the spread seen in Figure 5 (especially around [Fe/H] $\sim$ -1.5) as shown in Figure 7.

The decrease in carbon depletion rate for the nitrogen strong stars between Figures 6 and 7 depicts the large dependence on initial [C/Fe] with some rates changing as much as 20 dex/Gyr. With the carbon depletion rate having such a dependence on the initial [C/Fe], it is not possible to determine an exact carbon depletion rate for each cluster because the initial [C/Fe] for each star cannot be determined within the uncertainty required.

To precisely determine the Δ[C/Fe]/Δt for a star, one would need to evaluate the initial [C/Fe] for a RGB star before it began mixing. Determining the [C/Fe] and [N/Fe] for stars on the main sequence of a cluster, or just before the point of mixing (the subgiant or early giant phase), would provide information on which stars have been polluted with CN(O)-cycle material as well as an estimate for the initial [C/Fe] for nitrogen strong RGB stars. However, recent studies have shown that in some clusters the [C/Fe] and [N/Fe] abundances for main sequence and early turn-off stars spread over a wide range of abundances ($\sim$ 0.5 dex) rather than forming peaks around nitrogen strong and nitrogen normal abundances(Briley et al. 2004; Cohen, Briley, & Stetson 2005). Because of the range in initial [C/Fe] and [N/Fe] abundances before mixing has begun, values for the initial [C/Fe] of a star with the precision necessary to exactly determine Δ[C/Fe]/Δt may never be achievable because the large number of possible interactions in a globular cluster that affect a stars initial [C/Fe] are too great to exactly predict.

REFERENCES

Alcaino, G. 1972, A&A, 16, 220

Alcaino, G. 1978, A&AS, 33, 185

Alonso, A., Arribas, S., & Martinez-Roger, C. 1999, A&AS, 140, 261

Alonso, A., Arribas, S., & Martinez-Roger, C. 2001, A&A, 376, 1039

Arp, H. C. 1955, AJ, 60, 317

Bell, R. A., Paltoglou, G., & Tripicco, M. J. 1994, MNRAS, 268, 771

Briley, M. M., Harbeck, D., Smith, G. H., & Grebel, E. K. 2004, AJ, 127, 1588

Buonanno, R., Buscema, G., Corsi, C. E., Iannicola, G., & Fusi Pecci, F. 1983, A&AS, 51, 83

Carretta, E., Bragaglia, A., Gratton, R., et al. 2009, A&A, 505, 117

Carretta, E., Bragaglia, A., Gratton, R., & Lucatello, S. 2009, A&A, 505, 139

Cayrel de Strobel, G., Soubiran, C., & Ralite, N. 2001, A&A, 373, 159

Charbonnel, C., Brown, J. A., & Wallerstein, G. 1998, A&A, 332, 204

Charbonnel, C., & Zahn, J.-P. 2007, A&A, 476, L29

Cohen, J. G. 1999, AJ, 117, 2428

Cohen, J. G., Briley, M. M., & Stetson, P. B. 2005, AJ, 130, 1177

Cuffey, J. 1961, PGLO, 45, 364

Denissenkov, P. A., & Pinsonneault, M. 2008, ApJ, 684, 626

Dékány, I., & Kovács, G. 2009, A&A, 507, 803

Dickens, R. J. 1972, MNRAS, 157, 299

Eggleton, P. P., Dearborn, D. S. P., & Lattanzio, J. C. 2006, Sci, 314, 1580

Fusi Pecci, F., Ferraro, F. R., Crocker, D. A., Rood, R. T., & Buonanno, R. 1990, A&A, 238, 95

Gustafsson, B., Edvardsson, B., Eriksson, K., et al. 2008, A&A, 486, 951

Harris, W. E., & Racine, R., 1973, AJ, 78, 242

Harris, W. E., Racine, R., & de Roux, J. 1976, ApJS, 31, 13

Harris, W. E. 2010, arXiv, arXiv:1012.3224

Hatzidimitriou, D., Antoniou, V., Papadakis, I., et al. 2004, MNRAS, 348, 1157

Iben, I., Jr. 1965, ApJ, 142, 1447

Iben, I., Jr. 1968, ApJ, 154, 581

Johnson, C. I., Kraft, R. P., Pilachowski, C. A., et al. 2005, PASP, 117, 1308

Martell, S. L., Smith, G. H., & Briley, M. M. 2008, AJ, 136, 2522

Menzies, J. 1974, MNRAS, 168, 177

Meszaros, S., Dupree, A. K., & Szentgyorgyi, A. 2008, AJ, 135, 1117

Mészáros, S., Dupree, A. K., & Szalai, T. 2009, AJ, 137, 4282

Norris, J., Cottrell, P. L., Freeman, K. C., & Da Costa, G. S. 1981, ApJ, 244, 205

Prisinzano, L., Micela, G., Sciortino, S., Affer, L., Damiani, F., 2012, A&A 546, 9

Racine, R. 1971, AJ, 76, 331

Rey, S.-C., Lee, Y.-W., Byun, Y.-I., & Chun, M.-S. 1998, AJ, 116, 1775

Sandage, A. R. 1953, AJ, 58, 61

Sandage, A. R., & Walker, M. F. 1955, AJ, 60, 230

Sandage, A., & Katem, B. 1964, ApJ, 139, 1088

Sandage, A., Katem, B., & Johnson, H. L. 1977, AJ, 82, 389

Sandquist, E. L., & Bolte, M. 2004, ApJ, 611, 323

Sarajedini, A., & Layden, A. 1997, AJ, 113, 264

Sawyer Hogg, H. 1973, Publications of the David Dunlap Observatory, 3, 6

Skrutskie, M. F., Cutri, R. M., Stiening, R., et al. 2006, AJ, 131, 1163

Sweigart, A. V., & Mengel, J. G. 1979, ApJ, 229, 624

Yi, S., Demarque, P., Kim, Y.-C., et al. 2001, ApJS, 136, 417

Zoccali, M., Cassisi, S., Piotto, G., Bono, G., & Salaris, M. 1999, ApJ, 518, L49

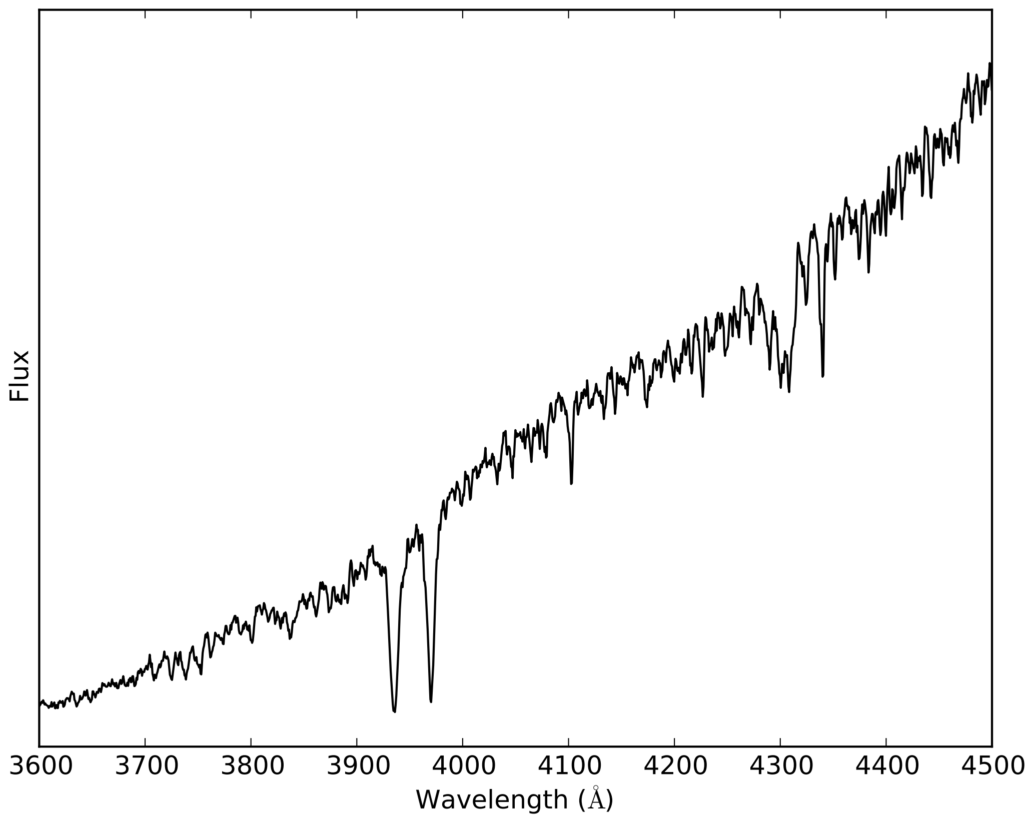

Fig. 1.— Shown above is a sample spectrum taken from the SOAR observations. The spectrum is a giant from M30, which has an [Fe/H] value of -2.27.(Harris, W. E. 2010) The CN and CH bands can be seen around 3800 and 4300, respectively.

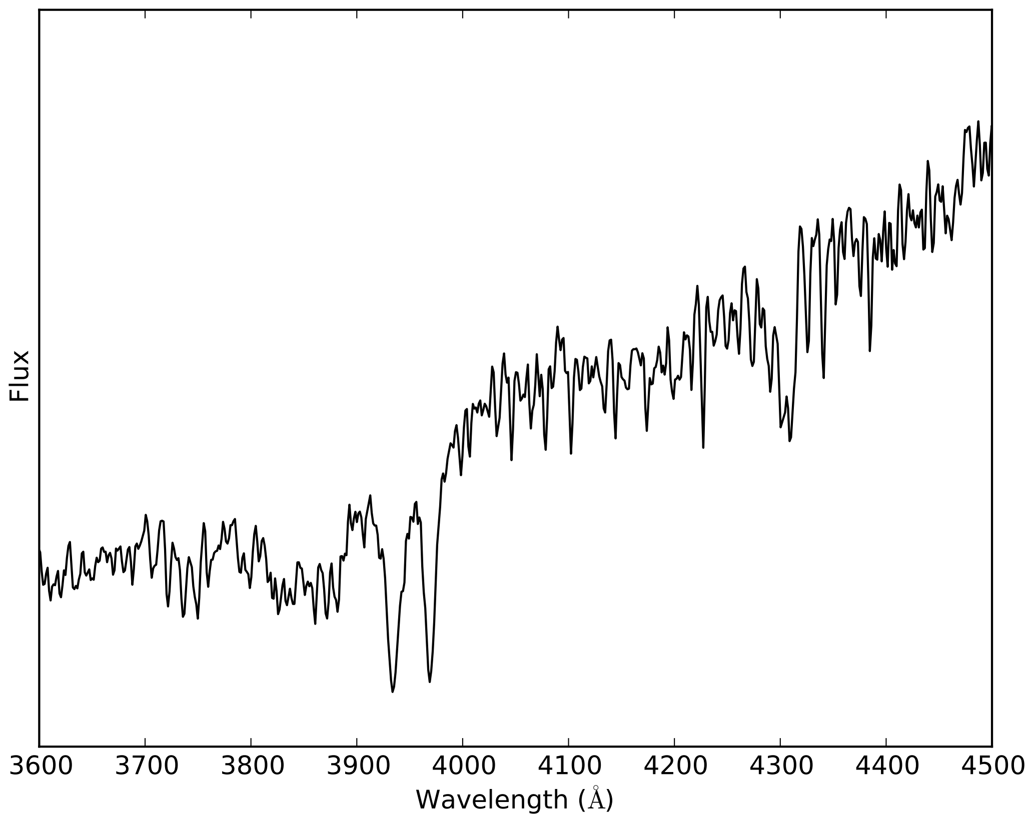

Fig. 2.— Shown above is a sample spectrum taken from the KPNO observations. The spectrum is a giant from M10, which has an [Fe/H] value of -1.56.(Harris, W. E. 2010) The CN and CH bands can be seen around 3800 and 4300, respectively.

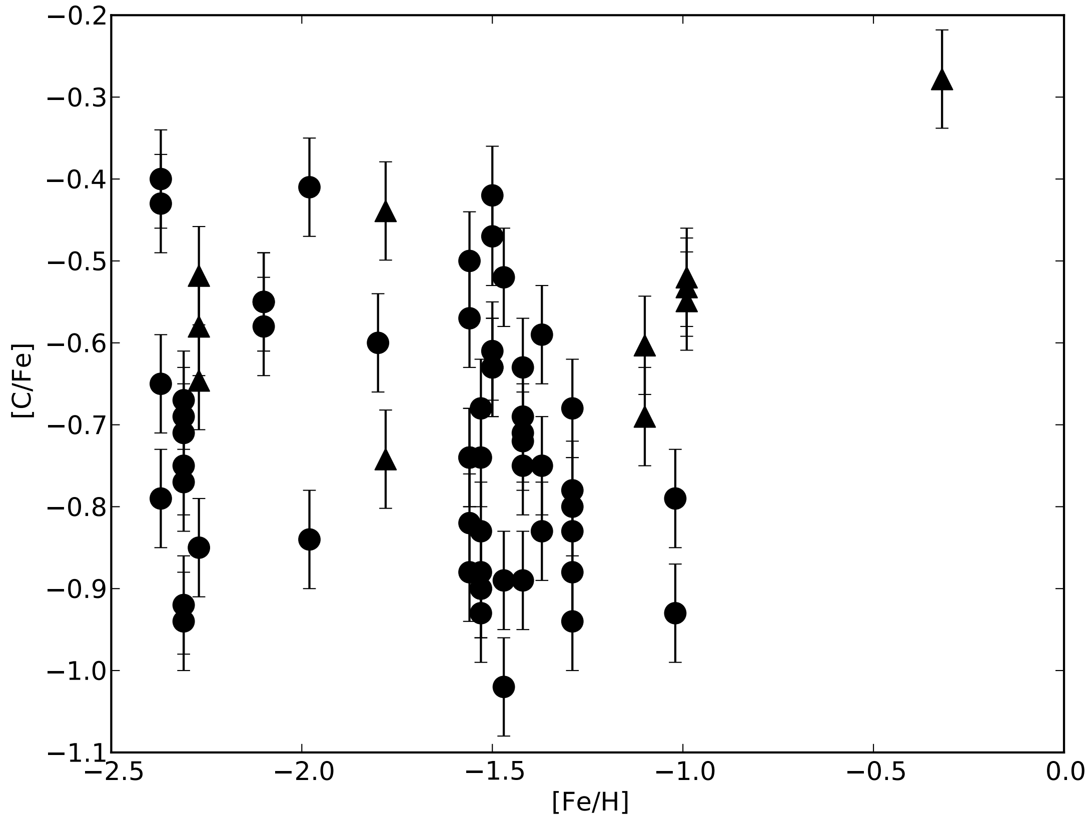

Fig. 3.— The figure above shows [C/Fe] versus [Fe/H] for each star in the sample. Circles indicate stars observed with KPNO and triangles are those observed with SOAR. No clear correlation between [C/Fe] and [Fe/H] can be seen in the plot above because each star's [C/Fe] depends on initial carbon abundance, the carbon depletion rate, and how long the star has been mixing.

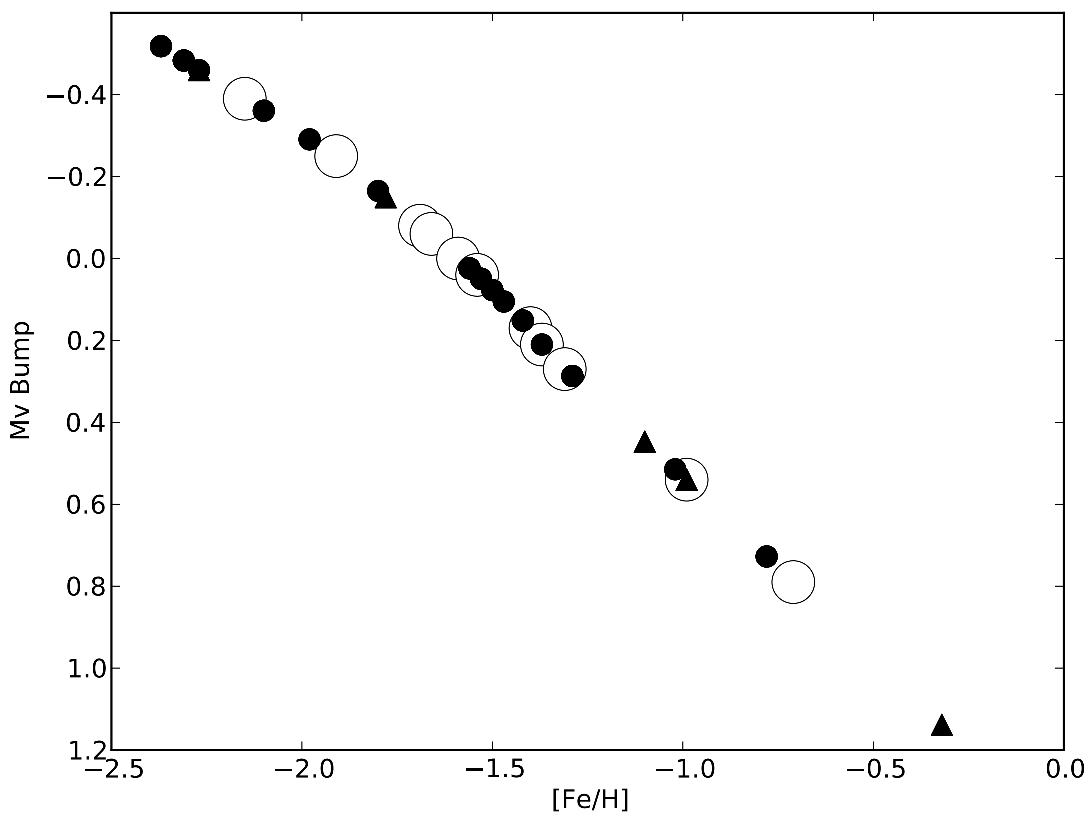

Fig. 4.— The figure above depicts the absolute magnitude of the luminosity function bump for each cluster as a function of metallicity. The open circles represent data from Fusi Pecci et al (1990) The solid circles represent clusters observed by the KPNO sample, and the triangles represent clusters observed by the SOAR sample.

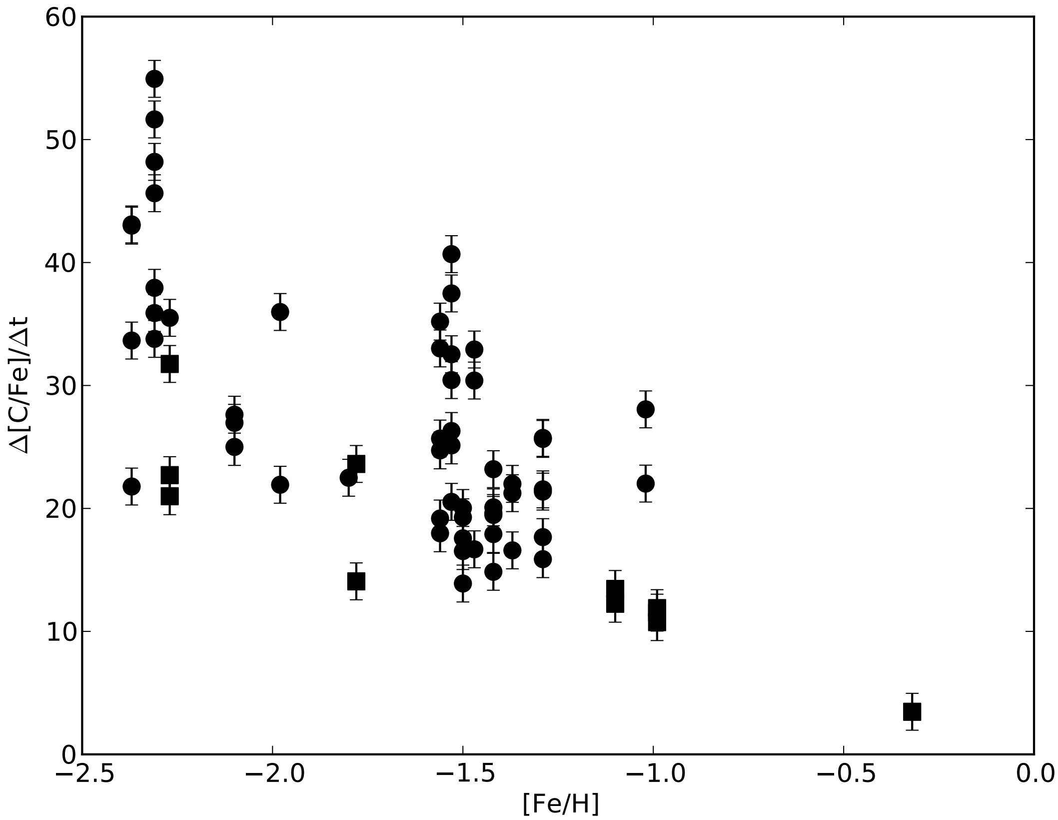

Fig. 5.— Shown above is the carbon depletion rate as a function of [Fe/H] for each member of our sample. Members from the SOAR observations are shown as squares and KPNO observations are shown as circles. A general decrease in carbon depletion rate is seen, but there is a large amount of scatter (especially around [Fe/H] $\sim$ -1.5).

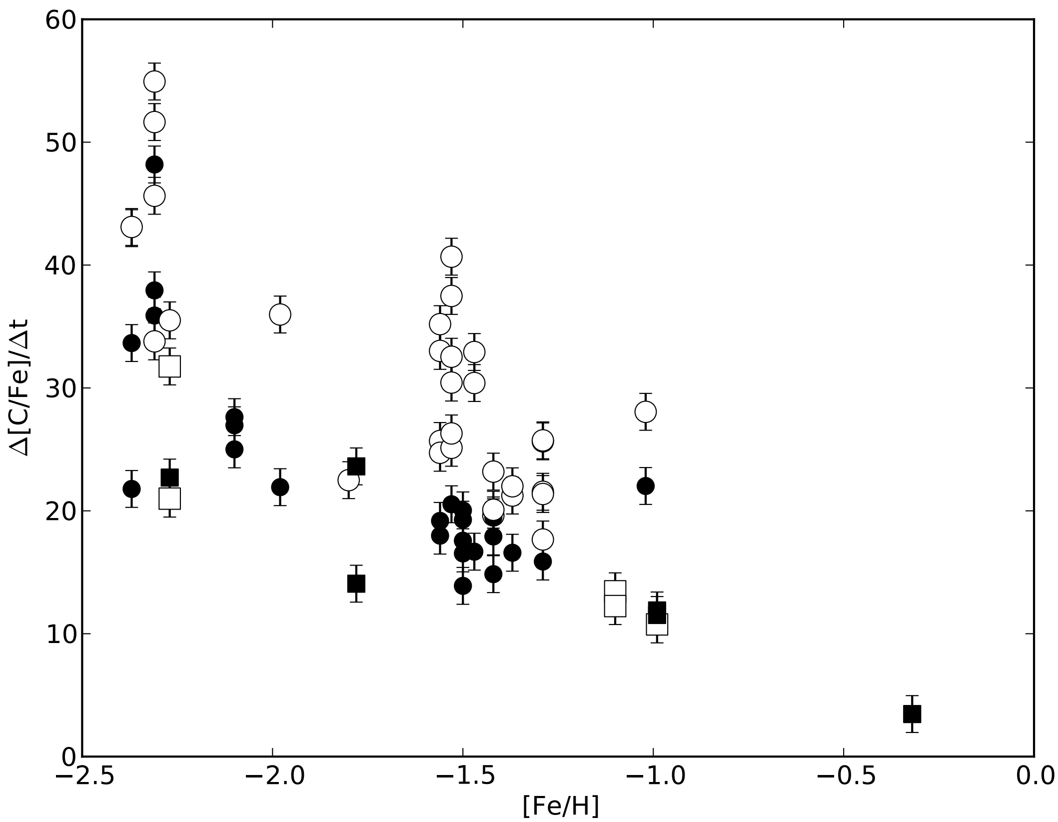

Fig. 6.— The figure above is the same plot as Figure 5, but the nitrogen strong stars are depicted as open circles for KPNO data and open squares for SOAR data. Likewise, filled circles and squares are nitrogen weak stars from each observatory.

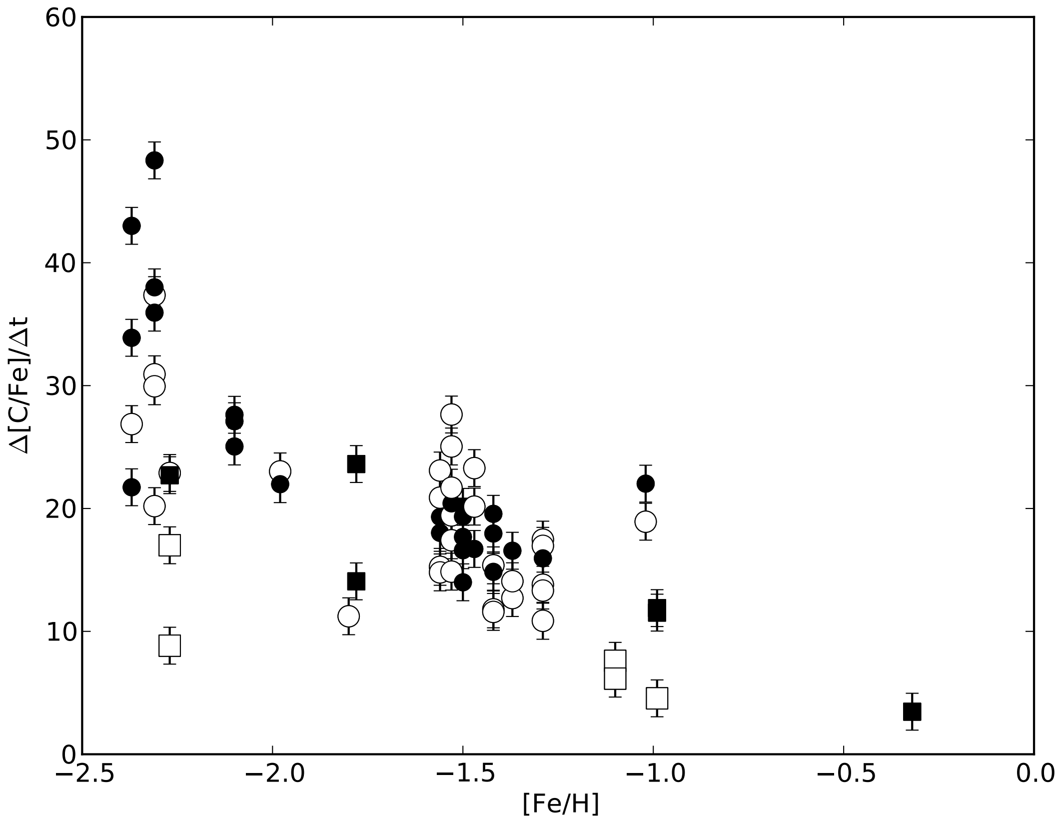

Fig. 7.— Shown above is a plot of carbon depletion rate as a function of metallicity, but the carbon depletion rates for the nitrogen strong stars have been lowered to account for their lower initial carbon abundance. The spread in carbon depletion rates for each cluster is reduced, especially around [Fe/H] $\sim$ -1.5. A large spread still exists at lower metallicities, which is caused by a larger uncertainty based on a stronger temperature dependence in the [C/Fe] abundances.

Table 1. Presented below are the values for V magnitude, temperature, [C/Fe] and [N/Fe] for each member star.

Globular Cluster	[Fe/H]	V	M_v	T_{eff} (K)	[C/Fe]	[N/Fe]
SOAR Stars						
NGC 6362[3]						
4	-0.99	13.32	-1.36	4328	-0.55	0.76
6	-0.99	13.23	-1.45	4216	-0.52	1.16
25	-0.99	13.32	-1.36	4108	-0.53	0.77
NGC 6723[4]						
1-5	-1.1	13.30	-1.54	3942	-0.69	2.22
2-4-62	-1.1	13.38	-1.46	4004	-0.60	1.69
NGC 7099 (M30)[5,6]						
PE-19	-2.27	13.04	-1.6	4537	-0.52	1.22
38	-2.27	13.24	-1.4	4642	-0.65	1.37
157	-2.27	13.00	-1.64	4419	-0.58	0.94
NGC 7492[7]						
R	-1.78	15.51	-1.59	4516	-0.44	0.93
T	-1.78	15.50	-1.6	4526	-0.74	0.91
Terzan 7[8]						
1681	-0.32	15.85	-1.16	4331	-0.28	0.54
KPNO Stars						
NGC 6254 (M10)[9,10,11,12]						
A-I-12	-1.56	13.13	-1.24	4405	-0.50	0.63
A-I-15	-1.56	12.92	-1.32	4383	-0.57	0.60
A-I-60	-1.56	13.17	-1.11	4405	-0.82	1.41
A-I-61	-1.56	13.08	-1.12	4635	-0.88	1.07
A-II-105	-1.56	12.94	-1.29	4372	-0.74	1.15
A-III-5	-1.56	12.71	-1.33	4421	-0.74	1.15
NGC 6218 (M12)[13,14]						
379	-1.37	12.59	-1.37	4221	-0.75	1.28

Table 1—Continued

Globular Cluster	[Fe/H]	V	M_v	T_{eff} (K)	[C/Fe]	[N/Fe]
423	-1.37	12.58	-1.38	4247	-0.59	0.61
i	-1.37	12.78	-1.47	3963	-0.83	1.46
NGC 6205 (M13)[9,10]						
I-23	-1.53	13.21	-1.12	4507	-0.93	0.95
I-24	-1.53	12.86	-1.47	4382	-0.74	1.01
I-42	-1.53	12.98	-1.35	4487	-0.83	1.23
II-33	-1.53	12.67	-1.66	4235	-0.68	0.85
III-52	-1.53	12.67	-1.66	4221	-0.88	1.32
IV-15	-1.53	12.96	-1.37	4491	-0.90	1.06
IV-34	-1.53	13.15	-1.18	4403	-0.90	1.38
NGC 7078 (M15)[10,15,16]						
292	-2.37	14.02	-1.39	4613	-0.65	0.80
363	-2.37	13.86	-1.57	4554	-0.79	1.43
51	-2.37	14.14	-1.25	4632	-0.43	0.68
90	-2.37	13.778	-1.58	5592	-0.40	0.87
NGC 5257 (M3)[17]						
AH	-1.50	13.44	-1.33	4569	-0.42	0.51
BF	-1.50	13.63	-1.45	4400	-0.63	0.54
I-46	-1.50	13.73	-1.25	4490	-0.47	0.47
IV-25	-1.50	13.60	-1.39	4364	-0.63	0.84
U	-1.50	13.49	-1.54	4405	-0.61	0.75
NGC 5904 (M5)[9,18]						
I-14	-1.29	13.00	-1.44	4259	-0.83	1.27
I-71	-1.29	13.08	-1.36	4298	-0.94	1.46
III-36	-1.29	12.81	-1.70	4176	-0.78	1.26
IV-34	-1.29	13.03	-1.40	4309	-0.80	1.14
IV-56	-1.29	13.21	-1.25	4325	-0.88	1.29

Table 1—Continued

Globular Cluster	[Fe/H]	V	M_v	T_{eff} (K)	[C/Fe]	[N/Fe]
IV-72	-1.29	12.85	-1.63	4221	-0.68	0.62
NGC 5024 (M53)[19,20,21]						
P	-2.10	14.83	-1.51	4519	-0.58	0.60
S3R4	-2.10	14.77	-1.54	4469	-0.55	0.67
V	-2.10	14.88	-1.43	4512	-0.55	0.60
NGC 6981 (M72)[6]						
10	-1.42	14.67	-1.64	4379	-0.75	1.03
12	-1.42	14.58	-1.73	4232	-0.72	0.60
16	-1.42	14.66	-1.65	4226	-0.89	1.41
17	-1.42	14.95	-1.36	4336	-0.63	0.48
18	-1.42	14.80	-1.51	4291	-0.71	1.16
6	-1.42	14.28	-2.03	4153	-0.69	0.66
NGC 6341 (M92)[15,22]						
120-IV-49	-2.31	13.06	-1.48	4599	-0.94	1.28
278-I-67	-2.31	13.32	-1.29	4598	-0.67	0.69
454-XI-80	-2.31	13.04	-1.65	4429	-0.92	1.19
458	-2.31	12.91	-1.73	4473	-0.77	0.73
550-XI-19	-2.31	12.87	-1.78	4480	-0.75	1.12
81-II-70	-2.31	13.08	-1.54	4555	-0.69	0.70
85-III-82	-2.31	13.33	-1.28	4566	-0.71	1.14
NGC 4147[23]						
II-44	-1.80	14.97	-1.52	4748	-0.60	1.03
NGC 5053[24]						
D	-2.27	14.44	-1.79	4464	-0.85	0.97
NGC 6171 (M107)[25]						
245	-1.02	13.76	-1.29	4074	-0.79	0.79
H	-1.02	13.89	-1.16	4008	-0.93	1.66

Table 1—Continued

Globular Cluster	[Fe/H]	V	M_v	T_{eff} (K)	[C/Fe]	[N/Fe]
NGC 6779 (M56)[27]						
20	-1.98	14.12	-1.56	4509	-0.84	1.23
24	-1.98	14.38	-1.30	4596	-0.41	0.66
NGC 6934[28]						
1-143	-1.47	14.96	-1.32	4357	-0.89	1.03
1-4	-1.47	14.88	-1.40	4233	-1.02	1.54
1-78	-1.47	14.87	-1.41	4287	-0.52	0.53

[3]Alcaino (1972), [4]Menzies (1974), [5]Alcaino (1978), [6]Dickens (1972)

[7]Cuffey (1961), [8]Sarajedini & Layden (1997), [9]Arp (1955)

[10]Carretta et al. (2009a), [11]Cayrel de Strobel et al. (2001)

[12]Harris et al. (1976), [13]Carretta et al. (2009b), [14]Racine (1971)

[15]Buonanno et al. (1983), [16]Meszaros et al. (2008), [17]Sandage (1953)

[18]Sandquist & Bolte (2004), [19]Dékány & Kovács (2009), [20]Rey et al. (1998)

[21]Sawyer Hogg (1973), [22]Mészáros et al. (2009), [23]Sandage& Walker (1955)

[24]Sandage et al. (1977), [25]Sandage & Katem (1964), [26]Hatzidimitriou et al. (2004)

[27]Harris, & Racine (1973)

Table 2. Presented below are the values for the change in [C/Fe] abundance using the SSG synthetic spectra based on changes in certain assumptions

Assumption Changed	Average Δ[C/Fe]
T_{eff} + 150 K	0.10
Solar [O/Fe]	-0.15
$C^{13}/C^{12} \sim +10$	0.02